Journal of
Materials Chemistry C

Accepted Manuscript

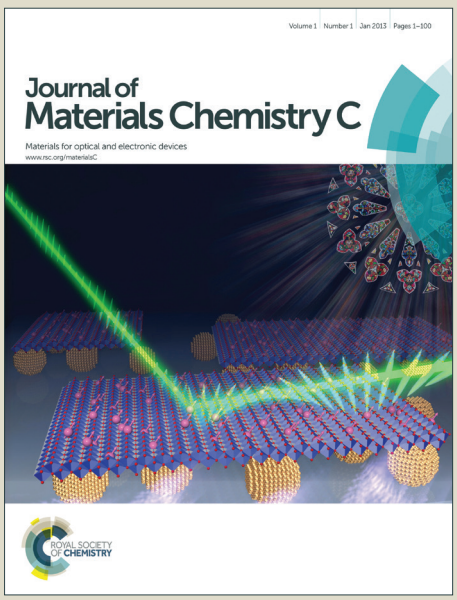

ROYAL SOCIETY OF CHEMISTRY

www.rsc.org/materialsC

Tailored design of $Co_xMn_{1-x}Fe_2O_4$ nanoferrites: a new route for dual control of size and magnetic properties

Carlos Fernandes,[a,†] Clara Pereira,[a,†] María Paz Fernández-García,[b] André M. Pereira,[c] Alexandra Guedes,[d] Rodrigo Fernández-Pacheco,[e] Alfonso Ibarra,[e] M. Ricardo Ibarra,[e] João P. Araújo,[*,b] and Cristina Freire[*,a]

[a] REQUIMTE, Departamento de Química e Bioquímica, Faculdade de Ciências, Universidade do Porto, 4169-007 Porto, Portugal

[b] IFIMUP and IN – Institute of Nanoscience and Nanotechnology, Departamento de Física e Astronomia, Faculdade de Ciências, Universidade do Porto, 4169-007 Porto, Portugal

[c] Blackett Laboratory, Imperial College London, London SW7 2AZ, United Kingdom

[d] Centro de Geologia e Departamento de Geociências, Ambiente e Ordenamento do Território, Faculdade de Ciências, Universidade do Porto, 4169-007 Porto, Portugal

[e] Laboratorio de Microscopías Avanzadas, Instituto de Nanociencia de Aragón, Universidad de Zaragoza, ES-50018 Zaragoza, Spain

*** Corresponding authors:**

Dr. Cristina Freire: Tel: +351 220402590; Fax: +351 220402659; e-mail: acfreire@fc.up.pt

Dr. João P. Araújo: Tel: +351 220402334; Fax: +351 220402406; e-mail: jearaujo@fc.up.pt

[†] Both authors contributed equally to this work.

Abstract

This work reports the tailored design of novel mixed ferrite nanoparticles, $Co_xMn_{1-x}Fe_2O_4$ (x = 0, 0.3, 0.7, 1) through an optimized one-pot aqueous coprecipitation process. The influence of the substitution between Mn(II) and Co(II) and of the alkaline agent, isopropanolamine (MIPA) or NaOH, on the morphological, chemical and magnetic properties of the nanomaterials was investigated. The joint action between chemical substitution and type of alkaline agent allowed a precise tuning of the particle size, magnetic properties and inversion degree of the spinel structure. A wide range of particle dimensions (from 3 to 30 nm) and saturation magnetization (from 57 to 71 emu g^{-1}) was achieved. The increase of Co(II) content from x = 0 to x = 1 led to a systematic decrease of the particle size, regardless of the base type, which could be modelled by an exponential decay function. For each Co:Mn composition, the use of MIPA instead of the traditional NaOH promoted a three times reduction of the particle size and simultaneously switched the magnetic state of the $Co_xMn_{1-x}Fe_2O_4$ nanomaterials from ferromagnetic to superparamagnetic. These results constitute a step forward in the challenging quest for high-performance magnetic nanoprobes by an eco-friendly synthesis route.

Keywords: coprecipitation, magnetic nanoparticles, isopropanolamine, cobalt ferrite, manganese ferrite, mixed ferrites

1. Introduction

Spinel-type ferrite nanoparticles (MFe_2O_4, where M(II) is a *d*-block transition metal) are promising building blocks for the development of new technologies owing to their remarkable magnetic, electrical and optical properties.[1–3] The possibility of changing the identity of the M(II) cation within the ferrite is a keystone feature to modulate the magnetic configuration, revolutionizing the world of modern technologies and fundamental science.[4,5] The ability to tailor their surface chemistry is another key parameter that allows engineering their characteristics en route to the target application.[1,6,7] In this context, this family of nanomaterials has been fostering innovation in a myriad of research areas especially in biomedicine,[1,8,9] catalysis,[10,11] environmental remediation,[12] magnetic refrigeration[13] and microwave technologies.[14]

Among the different spinel-type ferrite systems, special attention has been devoted to nanosized manganese(II) ferrite ($MnFe_2O_4$) and cobalt(II) ferrite ($CoFe_2O_4$) as alternatives to magnetite (Fe_3O_4) due to their higher chemical resistance to oxidation and intrinsic magnetic features.[15] $MnFe_2O_4$ has been gaining increased importance for biomedical applications (magnetic resonance imaging, biomolecule detection, magnetic hyperthermia) owing to its enhanced saturation magnetization when compared to other nanoferrites.[16–20] On the other hand, $CoFe_2O_4$ is among the preferred materials for high-density information storage and stress sensing applications due to its high coercivity and magnetocrystalline anisotropy.[18,21–23]

Nevertheless, the design of superparamagnetic Co(II)- and Mn(II)-based ferrite nanoparticles with structural, magnetic and electrical properties optimized to each type of application continues to be a challenging milestone for scientists and engineers. The rational design of nanoferrites with predictable, controllable and reproducible properties has been highlighted in several works, especially for industrial-scale production.[4,24–29]

Li *et al.* reported the synthesis of $MnFe_2O_4$ and $CoFe_2O_4$ nanomaterials with tunable size ranging from 3 to 20 nm prepared through the variation of the reaction conditions or by seed-mediated growth during the thermal decomposition process.[4] Zhang and co-authors developed a statistical method of factorial design to quantitatively correlate the size of $CoFe_2O_4$ nanoparticles with the experimental conditions used in the microemulsion process.[24] This chemometric model allowed the synthesis of spinel ferrite particles with predictable particle size over the range of 5 to 35 nm with a deviation of 1–3 nm. Systematic studies on the dependency of the magnetic properties of these spinel ferrite nanoparticles with size,[25] shape,[26] surface chemistry[27,28] and interparticle interactions[29] were also reported, namely their relation with the blocking temperature, saturation magnetization and coercivity of the nanomaterials.

More recently, the partial M(II) chemical substitution within these nanoferrites ($Co_xMn_{1-x}Fe_2O_4$ with x ranging from 0 to 1) emerged as a promising strategy to improve their performance. In fact, the potentialities of this strategy to improve the structure, surface disorder and/or magnetic properties have been highlighted for the synthesis of other mixed spinel systems such as $Zn_xMn_{1-x}Fe_2O_4$, $Zn_xFe_{1-x}Fe_2O_4$,[30] $Ni_{1-x}Zn_xFe_2O_4$,[31] etc. Various methods have been reported for the synthesis of $Co_xMn_{1-x}Fe_2O_4$ mixed ferrites such as ceramic method,[32,33] calcination of layered double hydroxide precursors,[34] thermal decomposition,[35] sol-gel combustion,[36] chemical autocombustion,[37,38] polyol method,[39–43] hydrothermal route,[44,45] solid-state reactions[46] and nonhydrolysis/seed-mediated growth method.[22] However, most of these routes required harsh conditions (high temperatures, organic solvents, post-treatments) or originated Co-Mn ferrites featuring large particle size (typically ranging from 20 nm to large grain sizes) and/or ferromagnetic properties. In this context, the quest for more sustainable and less time-consuming methods for the synthesis of $Co_xMn_{1-x}Fe_2O_4$ is still

being pursued. The coprecipitation stands up as a greener alternative since it requires low-cost reagents, aqueous conditions and can be easily scalable to industrial applications.[1,8,47]

To the best of our knowledge, scarce studies on $Co_xMn_{1-x}Fe_2O_4$ mixed ferrites prepared by coprecipitation have been reported,[48,49] with the particle dimensions still being a major limitation (28 nm–56 nm for x = 0.25–1 or 80 nm for x = 0.7). Additionally, the fine control of their magnetic properties through this route is still lacking.

In view of these challenges, in this work a new set of magnetic $Co_xMn_{1-x}Fe_2O_4$ (x = 0, 0.3, 0.7, 1) ferrite nanoparticles has been fabricated through an innovative one-pot aqueous coprecipitation route recently designed for the synthesis of simple MFe_2O_4 ferrites.[50] Through the progressive variation of the M(II) cation composition combined with the new coprecipitation agent isopropanolamine (MIPA), we endeavor to fine tune the particle size, saturation magnetization and inversion degree of the nanoferrites. MIPA has been recently reported as a potential alternative to traditional coprecipitation agents (NaOH, NH_3, tetraalkylammonium hydroxides, etc.) for the production of simple MFe_2O_4 nanoferrites,[50] since it can drastically reduce their particle size while improving their spin surface rearrangement thus enhancing the saturation magnetization and leading to superparamagnetic state at room temperature. The influence of the alkaline agent on the resulting properties of $Co_xMn_{1-x}Fe_2O_4$ is also addressed through their fabrication with NaOH. The architectured design of magnetic nanoparticles (MNPs) through this dual combination between chemical substitution and coprecipitation agent allows a systematic optimization of the morphological, structural and magnetic properties for each specific application. These are key parameters for the design of high-

performance magnetic nanoprobes for theranostics and imaging applications as well as for the miniaturization of modern electronic devices.

2. Experimental section

2.1 Reagents and solvents

Cobalt(II) chloride hexahydrate (≥99%), manganese(II) chloride tetrahydrate (≥99%), iron(III) chloride hexahydrate (≥98%) and sodium hydroxide (pellets, analytical grade) were purchased from Merck. Hydrochloric acid (37%, analytical grade) was from Panreac, aqueous tetramethylammonium hydroxide solution (TMAOH, 25%), 1-amino-2-propanol (MIPA, 93%) and potassium bromide (99%, spectroscopic grade) were purchased from Aldrich. Ultrapure water (Millipore, specific resistivity: 18 MΩ cm) was used throughout the experiments. All reagents and solvents were used without complementary purification.

2.2 Synthesis of $Co_xMn_{1-x}Fe_2O_4$ magnetic nanomaterials

The $Co_xMn_{1-x}Fe_2O_4$ nanoferrites containing different Co(II) and Mn(II) contents ($x = n_{Co(II)} / [n_{Co(II)} + n_{Mn(II)}] = 0, 0.3, 0.7, 1$), were prepared by a new coprecipitation method developed by our group, which in this work was extended to the fabrication of novel mixed nanoferrites.[50]

Briefly, stoichiometric quantities of $CoCl_2{\cdot}6H_2O$ and $MnCl_2{\cdot}4H_2O$ were separately dissolved in two solutions of 1 cm^3 of HCl (37%) in 4 cm^3 of water. In parallel, 20 mmol of $FeCl_3{\cdot}6H_2O$ were dissolved in 40 cm^3 of water. All solutions were heated at 50 ºC, mixed and then quickly added to 200 cm^3 of 3.0 M aqueous solution of MIPA at 90 ºC under vigorous mechanical stirring.

A black precipitate formed immediately and stirring was continued for 2 h at that temperature. Afterwards, the reaction mixture was cooled to room temperature and the precipitate was magnetically separated, washed several times with ultrapure water and dispersed in 0.1 M TMAOH aqueous solution. For comparison, the nanomaterials were also prepared using NaOH aqueous solution as alkaline agent.

For simplicity the samples are labelled as Co_xMn_{1-x}_M and Co_xMn_{1-x}_Na, where x = 0, 0.3, 0.7, 1, M stands for MIPA base and Na stands for NaOH base.

2.3 Physicochemical characterization

The metal contents were determined by atomic absorption spectroscopy (AAS) using a Philips PU 9200X device with a hollow cathode lamp of S & J Juniper & Co.

Transmission electron microscopy (TEM) was performed at the Advanced Microscopy Laboratory (LMA), Instituto Universitario de Nanociencia de Aragon (INA), Zaragoza, Spain, with T20 FEI TECNAI microscope operating at an accelerating voltage of 200 kV. A small amount of sample was dispersed in high purity ethanol under sonication. Afterwards, several drops of the resulting suspension were deposited on a holey carbon-film 400 mesh Cu grid and left to dry. After the evaluation of several TEM images, the diameter of ~270 particles was measured to generate histograms and calculate the average particle size and size distribution.

Powder X-ray diffraction (XRD) measurements were performed at Departamento de Química, CQ-VR, Universidade de Trás-os-Montes e Alto Douro (UTAD), Portugal, at room temperature using a PW 3040/60 X'Pert Pro Röntgen diffractometer with Cu $K\alpha$ radiation (λ = 1.5418 Å) and $\theta/2\theta$ Bragg-Brentano configuration, over the 2θ range of 20–80º. The system includes the ultrafast PW3015/20 X´Celerator detector and a secondary monochromator.

Raman spectra were recorded at room temperature on a Jobin-Yvon LabRaman spectrometer equipped with a CCD camera using a He−Ne laser at an excitation wavelength of 632.8 nm and a power of 20 mW. An Olympus optical microscope with a 50× objective lens was used to focus the laser beam on the sample and collect the scattered radiation. The laser power was reduced 50% with a neutral density filter to avoid thermal decomposition of the samples. The Raman spectra were fitted using the NGS LabSpec software, after a linear-type background subtraction.

Fourier transform infrared (FTIR) spectra were collected with a Jasco FT/IR-460 Plus spectrophotometer in the 4000–400 cm^{-1} range, using a resolution of 4 cm^{-1} and 32 scans. The spectra of the dried samples were obtained in KBr pellets containing 1 wt% of MNPs.

Thermogravimetric analysis (TGA) was carried out at LSRE/LCM, Departamento de Engenharia Química, Faculdade de Engenharia da Universidade do Porto, Portugal, on a Netzsch STA 409 PC/PG thermobalance, from 50 to 700 ºC, at a heating rate of 10 ºC min^{-1} under a nitrogen flow (50 cm^3 min^{-1}).

The isothermal magnetization (*M*) as a function of applied magnetic field (*H*) and zero-field-cooled/field-cooled (ZFC/FC) measurements were performed over the temperature range 5−370 K using a commercial Quantum Design superconducting quantum interference device (SQUID) magnetometer, with H up to 50 kOe.

3. Results and discussion

3.1 Tuning of the particle size and chemical composition

The stoichiometric composition of the magnetic nanoferrites was determined by AAS and the results are summarized in Table 1. For all $Co_xMn_{1-x}Fe_2O_4$ nanoferrites, the Co(II)/M(II) and M(II)/Fe(III) molar ratios (where $n_{M(II)} = n_{Co(II)} + n_{Mn(II)}$) are close to

the theoretical values, confirming the synthesis of the nanoferrites with the expected degree of cobalt substitution.

Table 1

The analysis of TEM micrographs (see representative images in Figure 1) clearly indicates that the aqueous coprecipitation using MIPA as alkaline agent leads to the formation of small-size quasi-spherical MNPs. The particle size distributions could be fitted by a log-normal function (Figure S1 in the Supplementary Information), leading to average particle sizes of 8.9, 6.7, 4.6 and 4.3 nm for Mn_M, $Co_{0.3}Mn_{0.7}$_M, $Co_{0.7}Mn_{0.3}$_M and Co_M samples, respectively (Table 1). In this context, the average particle size of Co_xMn_{1-x}_M MNPs decreases with the increase of Co(II) loading and the particle size distribution becomes narrower, especially for x up to 0.7.

Furthermore, the mixed Co-Mn nanoferrites prepared with MIPA present significantly smaller dimensions than those of the corresponding nanoferrites synthesized with NaOH (Table 1 and refs. 48 and 49). To the best of our knowledge, the particle sizes are even smaller than those of nanoferrites with similar Co(II):M(II) stoichiometry (x = 0.3 or 0.7) prepared by other methods reported in literature.[22,32,36,41,42,46] These results are in accordance with those recently reported for simple MFe_2O_4 MNPs prepared by coprecipitation using alkanolamine bases,[50] confirming the potential role of MIPA in the reduction of the particle size not only of simple but also of mixed nanoferrites.

Figure 1

The powder XRD patterns of all the nanomaterials were acquired in the 2θ range of 20–80º (Figure S2 in the Supplementary Information), in order to study their crystallographic structure and estimate their mean crystallite size.

The Bragg reflections match well with those of bulk ferrite standards, both in peaks position and relative intensities,[32,37,44,50] confirming the expected cubic spinel structure ($Fd\bar{3}m$). Additionally, no secondary peaks are detected in the XRD diffractograms of both single and mixed ferrites, indicating the formation of single phase nanomaterials during the one-step coprecipitation process. Therefore, neither the substitution of Mn(II) by Co(II) nor the alkaline coprecipitation agent (MIPA or NaOH) changes the expected crystallographic symmetry of $Co_xMn_{1-x}Fe_2O_4$ MNPs.

The mean crystallite diameter, D_{XRD}, was also calculated by XRD, using the Williamson-Hall relation in order to take into account the eventual contribution from internal strains:[50]

$$\beta_{total} = \beta_{size} + \beta_{strain} = \frac{K\lambda}{d_{\mathrm{XRD}} \cos\theta} + 4\eta \tan\theta \qquad (1)$$

where β_{total} is the full width at half-maximum of the XRD peak, K is the Debye-Scherrer constant (~0.94 for spherical NPs), λ is the incident X-ray wavelength, θ is the diffraction angle and η is the microstrain parameter. In the case of the internal microstrain, the values obtained from the Williamson-Hall plots (Figure S3 in the Supplementary Information) for all the samples were lower than 1%, indicating that the nanomaterials can be considered strain-free.[51,52]

The D_{XRD} values are in accordance with those determined by TEM (Table 1 and Figure 2), confirming that the $Co_xMn_{1-x}Fe_2O_4$ particle size decreases from x = 0 to x = 0.7 and then becomes practically constant.

Figure 2

For both MIPA- and NaOH-based materials, the particle size reduction ongoing from $MnFe_2O_4$ to $CoFe_2O_4$ follows a similar profile, suggesting an exponential decay. Based on this tendency, for both sets of nanomaterials the D_{XRD} *versus* x data were modeled using an exponential decay function given by:

$$D = D' + A \exp^{-\frac{x}{x_c}} \quad (2)$$

From Figure 2, a good accordance between the fitted curves and the experimental data can be observed. From the fitted values (see Figure 2) we can unveil the physical meaning of the different parameters. *D'* represents the minimum particle size which can be reached during the coprecipitation reaction (3.2 and 9.7 nm for MIPA and NaOH, respectively). The decay profile of the curves is expressed by the magnitude of the x_c parameter. For both sets of nanomaterials synthesized with MIPA and NaOH, the decay profiles are almost similar (x_c ~ 0.19), which is an evidence that this behavior is independent of the alkaline agent. In this context, x_c represents the influence of the Co(II):M(II) molar ratio on the size of $Co_xMn_{1-x}Fe_2O_4$ MNPs prepared by coprecipitation. This finding allows us to conclude that, in the present case, the Co(II):M(II) molar ratio is intrinsically responsible for the similar variation of the particle size, being independent of the synthesis conditions namely of the type of coprecipitation agent. In contrast, the *A* parameter presents distinct values for both MIPA and NaOH sets (6.9 and 21.3 nm, respectively), thus depending on the type of coprecipitation agent and, consequently, on the coprecipitation mechanism when using distinct alkaline agents.

Hence, a major breakthrough is that the determination of the *D(D', A,* x_c*)* dependence as a function of x for a specific base allows a precise control of the particle

size experimentally, by selecting the adequate Co(II):M(II) ratio during the coprecipitation procedure.

Finally, it is noteworthy that the ratios between D'_{MIPA}: D'_{NaOH} and A_{MIPA}:A_{NaOH}, are ~1:3, revealing that for all $Co_xMn_{1-x}Fe_2O_4$ compositions (x values), the addition of MIPA instead of NaOH leads to a 3 times particle size reduction. This outcome can be explained by the complexing properties of MIPA combined with its lower basicity (pH 10−11 *versus* pH 14 for NaOH aqueous solution). In fact, it has been recently reported that the dimensions of simple MFe_2O_4 MNPs prepared by coprecipitation could be greatly reduced when MIPA was employed instead of the inorganic NaOH base or other traditional bases reported in literature (e.g. ammonia, tetraalkylammonium hydroxides).[50,53,54] The alkanolamine not only acts as coprecipitation base but also as chelating agent due to its affinity to form coordination compounds with 3*d* divalent cations (coordination of nitrogen and oxygen atoms of MIPA with the subcoordinated metal atoms on the MNP surface), restraining the particle growth.[50,55]

The lattice parameter of the cubic unit cell, *a*, was calculated by the Bragg law using the (311) reflection (Table 1).[56] For both Co_xMn_{1-x}_M and Co_xMn_{1-x}_Na sets of nanomaterials, the *a* value decreases with the increase of Mn(II) substitution, which is in accordance with the tendency reported for their bulk counterparts (8.499 Å for $MnFe_2O_4$, JCPDS card no. 10-0319 and 8.391 Å for $CoFe_2O_4$, JCPDS card no. 22-1086). This behavior can be directly inferred through the comparison between the different diffractograms. All Bragg reflections are shifted towards higher 2θ angles ongoing from $MnFe_2O_4$ (x = 0) to $CoFe_2O_4$ (x = 1), regardless of the base type. This is especially noticed for (333) and (440) reflections, as illustrated in Figure 3A for Co_xMn_{1-x}_M nanomaterials.

Figure 3

When plotting the lattice parameter *a* as a function of the cobalt content x (Figure 3B), a linear tendency is observed for both MIPA- and NaOH-based MNPs which follows the Vegard's law.[57] This Vegard-like behavior can be assigned to the progressive substitution of Mn(II) ions with larger ionic radii (0.83 Å) by the smaller Co(II) cations (0.78 Å), in accordance with literature.[37,38,58]

To provide more insights on the MNPs atomic structure, all the materials were characterized by Raman spectroscopy, which is a powerful tool to extract information concerning the internal structure and bonding of nanomaterials.[59] In particular, Raman spectroscopy and/or Mössbauer spectroscopy have been used as complementary techniques for the structural characterization of spinel-type nanomaterials, especially when the corresponding XRD patterns are similar.[59–61]

The Raman spectra of the nanoferrites prepared with MIPA and NaOH are presented in Figure 4. As a result of the small particle size, some weak Raman modes and peak broadening are observed. Therefore, for a more accurate analysis, all spectra were deconvoluted and the obtained results are presented in Table S1 and Figure S4 in the Supplementary Information.

Figure 4

All spectra exhibit the five Raman active phonon modes typical of ferrites with spinel-type cubic structure *Fd3m*: A_{1g} (648–680 cm^{-1}), $3T_{2g}$ (539–565, 449−471 and 163−177 cm^{-1}) and E_g (278−293 cm^{-1}).[60,62–64] Besides these bands, from the spectra deconvolution, two additional Raman active modes are detected around 594–624 cm^{-1} and 328–371 cm^{-1} due to quantum-size effects.[60] Since the particles dimensions are

significantly smaller than the exciting radiation wavelength, there is a breakdown of the momentum conservation law, leading to the appearance of these extra phonon modes.

For both MIPA and NaOH sets, ongoing from pure $MnFe_2O_4$ to pure $CoFe_2O_4$, an increase of the intensity of the band at ~450 cm^{-1} relative to those above 600 cm^{-1} is clearly noticed. Additionally, the relative intensity of the band at 649–680 cm^{-1} *versus* that at 594–624 cm^{-1} changes, giving rise to a doublet-like shape in $Co_{0.7}Mn_{0.3}Fe_2O_4$ and $CoFe_2O_4$ (Figure 4).

Several authors assign the T_{2g} mode at 449–471 cm^{-1} to the local lattice vibrations of the ions in the octahedral sites and the bands above 600 cm^{-1} to $A_{1g}(1)$ and $A_{1g}(2)$ modes reflecting the vibrations within tetrahedral sites.[65–67] Furthermore, it is stated that bulk $MnFe_2O_4$ and $CoFe_2O_4$, although presenting a spinel structure, differ in the cations distribution among octahedral and tetrahedral sites.[61] Bulk $MnFe_2O_4$ presents a partially inverted spinel structure with Mn(II) cations predominantly occupying the tetrahedral sites, leading to a low inversion degree (~0.2, *i.e.* 20% of Mn(II) cations in octahedral sites). In contrast, $CoFe_2O_4$ presents a significantly higher inversion degree (~0.8), with Co(II) cations mainly occupying the octahedral positions and Fe(III) cations distributed between the octahedral and tetrahedral ones.

In this context, the change on the area and intensity of the band related with the octahedral sites relative to the bands associated with the tetrahedral A_{1g} modes ($A_{1g}(1)$ and $A_{1g}(2)$ bands) ongoing from $MnFe_2O_4$ to $CoFe_2O_4$ suggests a progressive increase of the degree of inversion of the spinel lattice, *i.e.* a different distribution of the divalent and trivalent cations between the tetrahedral and octahedral sites. The A_{1g} splitting also suggests the cations migration within both positions.[64,68,69]

More remarkably, for the simple nanoferrites, the area ratio between the bands associated with the octahedral ($A_{T2g(1)}$) and tetrahedral sites ($A_{A1g(1)}+A_{A1g(2)}$), *i.e.*

$A_{T2g(1)}/[A_{A1g(1)}+A_{A1g(2)}]$, is very similar to the corresponding degree of inversion predicted for their bulk counterparts, indicating the existence of a relation between these two parameters (Figure 5). Consequently, for both MIPA and NaOH series, the nanomaterials with x = 0.7 and x = 1 are those that present the highest degree of inversion whereas for Mn-enriched MNPs the inversion degree will be lower.

Figure 5

The importance of Raman spectroscopy to unveil the degree of inversion of transition metal ferrites has been highlighted by several authors in the last decade.[59,69–71] However, most of the studies only addressed the case of simple ferrites, whereas complete vibrational data for mixed metal oxides is still lacking. Wiglusz and co-authors prepared a series of simple MFe_2O_4 (M = Mn(II), Fe(II), Co(II) and Ni(II)) nanoferrites and correlated the presence of additional A_{1g} modes in their Raman spectra and their relative intensities to the degree of inversion.[69] The authors concluded that $MnFe_2O_4$ presented the lowest site inversion since the secondary A_{1g} mode exhibited the lowest intensity. In a similar study, Merino *et al.* related the multiplicity of the high-frequency A_{1g} Raman band with the different cation distribution in poly- and single crystals of $NiAl_2O_4$ spinels.[70] The relation between the A_{1g} splitting and the site occupancy was recently addressed for the mixed system of zinc-magnesium ferrites, $Zn_xMg_{1-x}Fe_2O_4$ (x = 0–1).[71]

However, those publications only addressed the inversion degree in terms of the differences on the relative intensities of the high-frequency A_{1g} modes. Although the changes in the intensity of the T_{2g} mode could be clearly observed in the reported Raman spectra, they were neglected. Since the T_{2g} mode at 449–471 cm^{-1} is assigned to vibrations within octahedral sites whereas the A_{1g} modes are associated with vibrations

within tetrahedral sites, we highlight that the contribution from the T_{2g} mode should also be considered for the analysis of the degree of inversion. In fact, the importance of relating both types of vibration modes with the changes in cation occupancy has been highlighted by Fuller *et al.*, for the systematic study of the Raman spectra of the titanomagnetite series, $Fe_{3-x}Ti_xO_4$ (x = 0.0, 0.2, 0.4, 0.6), which corroborates our statements.[72]

All the nanomaterials were also characterized by FTIR spectroscopy in order to provide additional information concerning their chemical structure and the presence of organic groups at their surface. The FTIR spectra of the $Co_xMn_{1-x}Fe_2O_4$ MNPs (Figure S5 in the Supplementary Information) exhibit a strong band in the range of 598–578 cm^{-1} assigned to M_{Td}–O stretching vibrations of the spinel lattice (M_{Td} = metal ions in tetrahedral sites).[73–75] The band associated with M_{Oh}–O stretching vibrations (M_{Oh} = metal ions in octahedral sites) could not be detected since it is beyond the detection limit of our FTIR equipment (<400 cm^{-1}). Upon the substitution of Mn(II) by Co(II) ions (from x = 0 to x = 1), there is a shift of the M_{Td}-O band to higher wavenumbers (from 578 to 593 cm^{-1} for MIPA series, and from 578 to 588 cm^{-1} for the NaOH congeners). This fact is probably related to differences in the metal cations distribution between the tetrahedral and octahedral sites of the ferrites lattice,[74] in accordance with Raman analysis.

Additionally, all FTIR spectra present a broad band around 3400–3390 cm^{-1} and a shoulder at ~1595 cm^{-1} due to O–H stretching and bending vibrations, respectively, of surface hydroxyl groups and physically adsorbed water.[73,75,76] Besides these features, several bands are detected in the ranges of 3018–2926 cm^{-1} and 1559–850 cm^{-1}, which are assigned to the characteristic stretching and bending vibration modes of TMAOH

and/or MIPA (for MIPA-based samples),[76–78] indicating their adsorption on the nanomaterials surface, in accordance with literature.

3.2 Magnetic properties

To provide information about the magnetic properties, the magnetization of all samples was measured at 300 K as a function of applied magnetic field up to 50 kOe (Figure 6).

Figure 6

Since the room temperature $M(H)$ curves present unsaturated behavior due to thermal fluctuations, the M_S values reported in Table 2 were calculated by extrapolation of M *vs.* $1/H$ ($H \rightarrow \infty$). Moreover, absolute M_S values arising from the contribution of the inorganic magnetic component (M_S^{inorg}) were determined (Table 2), taking into account the diamagnetic organic content quantified by TGA (see values in Table 1).

Table 2

The $M(H)$ curves of the samples synthesized with the alkanolamine (Figure 6A) reveal the absence of coercive field (H_C) and remanent magnetization (M_R), indicating that the nanomaterials are superparamagnetic at room temperature. In contrast, the Co_xMn_{1-x}_Na counterparts are ferromagnetic at the same temperature as revealed by non-zero H_C and M_R values (Figure 6B), which highlights the advantages of MIPA as coprecipitation agent to prepare nanomaterials with superparamagnetic properties.

Since the MIPA-based nanomaterials are superparamagnetic at room temperature, they can be interpreted as simplified systems of non-interacting magnetic monodomains with uniaxial anisotropy. In this context, it is possible to determine their magnetic core

size, size distribution and effective magnetic moment, by fitting the $M(H)$ curves with the Langevin law:[79]

$$M(H,T) = \int \mu \left(\coth\left(\frac{\mu H}{k_B T} \right) - \frac{k_B T}{\mu H} \right) f(\mu) d\mu \quad (3)$$

where μ is the magnetic moment per particle, T is the temperature, k_B is the Boltzmann constant and $f(\mu)d\mu$ represents the log-normal distribution of magnetic moments directly arising from the particle size distribution.

The obtained magnetic monodomain dimensions (D_{Lan}) and effective magnetic moments (M_S^{Lan}) are summarized in Tables 1 and S2 in the Supplementary Information, respectively. The D_{Lan} values are in accordance with those estimated by XRD, albeit being slightly higher due to the existence of magnetic dipolar interactions and/or anisotropy effects.[80–82] The saturation magnetization values resulting from Langevin analysis are also comparable to those obtained by extrapolation of M *vs.* $1/H$ ($H \rightarrow \infty$).

For the MIPA-based series, the M_S values at 300 K reveal that the nanomaterials with higher Mn(II) content present the highest magnetic response (M_S^{inorg} ~ 60.7 and 67.5 emu g^{-1} for Mn_M and $Co_{0.3}Mn_{0.7}$_M, respectively). On the other hand, for Co_xMn_{1-x}_Na set, $Co_{0.7}Mn_{0.3}$_Na exhibits the highest M_S. However, since the magnetic properties are strongly dependent on the particle size and, consequently, on the surface area to volume ratio, for a direct comparison between the magnetic properties of the nanostructures prepared with the different bases, the M_S/D_{XRD} values should be compared instead. In particular, this relation between M_S (near room temperature) and particle size is of tremendous importance for biotechnological applications to evaluate the nanomaterials performance.[20,21,83] In this context, the M_S/D_{XRD} values as a function of x were determined and are plotted in Figure 7. For both Co_xM_{1-x}_M and Co_xMn_{1-x}_Na sets, the results follow similar trends, with $Co_{0.7}Mn_{0.3}Fe_2O_4$ presenting the highest

M_S/D_{XRD} values. Interestingly, the $A_{T2g(1)}/[A_{A1g(1)}+A_{A1g(2)}]$ ratio determined from Raman analysis (Figure 5) exhibited a similar tendency. This resemblance suggests a relation between the magnetic properties and the ferrites cation distribution.

Figure 7

To provide a thorough understanding of the magnetic properties nature of the room temperature superparamagnetism of the nanomaterials prepared with MIPA, *M*(H) measurements at 5 K were performed (Figure 8) in order to neglect the contribution from spin wave thermal fluctuations.

Figure 8

From the *M*(*H*) curves at 5 K, it is observed that all the Co_xMn_{1-x}_M nanomaterials present a large magnetic hysteresis at that temperature typical of ferromagnetic nanoparticles in a blocked state. Moreover, the M_S values at 5 K decrease with the increase of Co content. This progressive reduction arises from the substitution of Mn(II) with S = 5/2 by Co(II) with S = 3/2 and and from the contribution of surface effects that are intrinsic to the scaling down of the nanomaterials dimensions (from 10 nm to 4 nm ongoing from x = 0 to x = 1, respectively). More importantly, when normalizing the *Ms* values at 5 K to D_{XRD} we achieve a similar tendency to that observed at 300 K, with the $Co_{0.7}Mn_{0.3}Fe_2O_4$-based nanomaterials presenting the highest M_S/D_{XRD} values (Figure 9A).

Figure 9

For both MIPA and NaOH sets of nanomaterials, the coercive field (H_C) values measured at 5 K increase ongoing from x = 0 to x = 1 (Figure 9B), which is related with

the enhancement of the effective anisotropy constant (K_{eff}) arising from the progressive Mn substitution by Co within the nanoferrite (K_{eff} ~10^4 erg cm^{-3} and ~10^6 erg cm^{-3} for bulk $MnFe_2O_4$ and $CoFe_2O_4$, respectively).[79] The particle size also plays an important role in K_{eff} adding a surface contribution as expressed by the following equation:

$$K_{eff} = K_{bulk} + K_S/D \quad (4)$$

From Figure 9B, when comparing the H_C values of MIPA and NaOH-based MNPs, although they follow the same tendency upon Mn substitution by Co, for each x composition the MIPA-based nanomaterial presents systematically higher H_C than the NaOH analog due to its significantly smaller particle size. This is especially highlighted in the case of x = 1, where the H_C values of Co_M and Co_Na present the highest discrepancy, due to the significant difference between their particle size. In this context, the particle dimensions have a dominant role on the K_{eff} values, and consequently, on the corresponding H_C. Since MIPA-based nanomaterials present smaller size than the NaOH congeners, the second term of eq. 4 (surface contribution) will dominate K_{eff}.

In the case of the superparamagnetic MIPA-based nanomaterials, the blocking temperature values (T_B) were estimated from the *M(T)* curves in the range of 5 to 370 K in the ZFC and FC regime (Figure 10), through the derivative maximum of the difference between the ZFC and FC curves. A progressive decrease of T_B can be observed from x = 0.3 to x = 1 (Figure 9B), which is opposite to what would be expected when considering only the magnetocrystalline anisotropy trend since $T_B \propto K_{eff}.D^3$. Nevertheless, as Song and co-authors recently reported,[22] this tendency is only valid if the particle dimensions remain constant regardless of the Co-Mn stoichiometry. This allows to conclude that it is the mean size of MIPA-based MNPs that is playing the major role on the observed T_B *vs.* Co content behavior (Figure 9B). The Mn_M sample is an exception to this trend since it presents the lowest T_B (estimated by the M(H) at

different temperatures, not shown). Still, we remark that among the MIPA series, Mn_M is the nanomaterial with the largest diameter (~10 nm) and thus its T_B value will be constrained by the K_{eff} contribution (which is 2 orders of magnitude lower than that of $CoFe_2O_4$ for bulk ferrite counterparts). In the case of the NaOH samples, their ferromagnetic nature at room temperature only arises from their significantly larger particle size (up to 3 times).

Figure 10

Finally, an additional feature – kink – is observed in the low temperature *M(H)* curve of all the Co-containing NaOH-based samples (x = 0.3 to 1, Figure S6 in the Supplementary Information), whereas in the case of the MNPs prepared with MIPA they were absent except for Co_M (Figure 8D) which presents an almost insignificant kink. Similar features were reported by Zeng *et al.*,[84] for a Fe_3O_4-$Fe_{58}Pt_{42}$ nanocomposite, where they were assigned to the spatial segregation of $Fe_{58}Pt_{42}$ and Fe_3O_4, resulting in the formation of large Fe particles, which was expressed in a two-phase behavior in the hysteresis loop. In our work, the detailed structural characterization of the samples (by XRD, Raman spectroscopy and TEM) revealed that both MIPA- and NaOH-based nanomaterials presented similar properties with no evidence of core-shell like structure or phase segregation. Therefore, we attribute the kinks in the *M*(*H*) curves of the NaOH-based materials at 5 K to the larger particle size, which leads to clustering, resulting in a two-phase behavior in the hysteresis loop. In contrast, in the case of MIPA, this effect is not perceptible, probably due to the particle size reduction combined with the existence of MIPA coordinated to the surface of the nanoparticles, which prevents the clustering effect. These results thus suggest that the

replacement of NaOH by the chelating base not only has an important role on the particles size reduction but also on the control of the magnetic anisotropy.

4. Conclusions

Novel mixed $Co_xMn_{1-x}Fe_2O_4$ MNPs with tailored particle size, inversion degree and saturation magnetization were produced for the first time by a one-pot eco-friendly coprecipitation process. Through the joint conjugation between M(II) substitution and base type, a fine-tuned control of particle dimensions ranging from 3 to 31 nm and of M_S from 57 to 71 emu g^{-1} was achieved at room temperature. Additionally, the use of the alkanolamine MIPA agent instead of NaOH boosted a switch of the magnetic nature of the nanomaterials from ferromagnetic to superparamagnetic at room temperature. Furthermore, at low temperatures the MIPA base promoted the tuning of the magnetic coercivity through the enhancement of the surface anisotropy constant contribution to K_{eff} as a result of the size reduction.

Finally, a correlation between M_S/D and the Co content was established for both MIPA- and NaOH-based nanomaterials, with MIPA promoting an enhancement of M_S/D up to 2.8 times at room temperature, with $Co_{0.7}Mn_{0.3}$_M and Co_M presenting the highest M_S/D values and simultaneously superparamagnetic properties. This architectured design is a crucial stepping stone for diversified technological applications. In particular, the superparamagnetism combined with optimized M_S/D values is highly desirable for biomedical purposes such as MRI and magnetic hyperthermia since it can reduce the required nanoprobe dosage level while preventing the MNPs aggregation in dispersion arising from magnetic dipolar interactions.

Acknowledgments

This work was funded by Fundação para a Ciência e a Tecnologia (FCT) and FEDER through grant no. PEst-C/EQB/LA0006/2011 and through project ref. PTDC/QUI-QUI/105304/2008 in the framework of Program COMPETE. The authors also acknowledge Operations NORTE-07-0124-FEDER-000067 – NANOCHEMISTRY and NORTE-070124-FEDER-000070 funded by FEDER and CCDRN as well as Interreg IV B SUDOE through Transpyrenees Action on Advanced Infrastructures for Nanosciences and Nanotechnologies (Train^2) project. The authors thank Prof. J. L. Figueiredo and Prof. M. F. R. Pereira from LSRE/LCM for access to the TGA equipment and Prof. P. Tavares and MSc. L. Fernandes from UTAD for the XRD measurements. C. F. and M. P. F.-G. (SFRH/BPD/87430/2012) thank FCT for their grants. A. I. acknowledges the Gobierno de Aragón (Grants E81) and the European Social Fund.

References

1 1 L. H. Reddy, J. L. Arias, J. Nicolas and P. Couvreur, *Chem. Rev.*, 2012, **112**, 5818.

2 2 C. Sun, J. S. H. Lee and M. Zhang, *Adv. Drug Deliv. Rev.*, 2008, **60**, 1252.

3 3 U. Jeong, X. Teng, Y. Wang, H. Yang and Y. Xia, *Adv. Mater.*, 2007, **19**, 33.

4 S. Sun, H. Zeng, D. B. Robinson, S. Raoux, P. M. Rice, S. X. Wang and G. Li, *J. Am. Chem. Soc.*, 2004, **126**, 273.

5 V. Šepelák, A. Feldhoff, P. Heitjans, F. Krumeich, D. Menzel, F. J. Litterst, I. Bergmann and K. D. Becker, *Chem. Mater.*, 2006, **18**, 3057.

6 N. Lee and T. Hyeon, *Chem. Soc. Rev.*, 2012, **41**, 2575.

7 A.-H. Lu, E. L. Salabas and F. Schüth, *Angew. Chem., Int. Ed.*, 2007, **46**, 1222.

8 M. Colombo, S. Carregal-Romero, M. F. Casula, L. Gutiérrez, M. P. Morales, I. B. Böhm, J. T. Heverhagen, D. Prosperi and W. J. Parak, *Chem. Soc. Rev.*, 2012, **41**, 4306.

9 F. Hu and Y. S. Zhao, *Nanoscale*, 2012, **4**, 6235.

10 D. Zhang, C. Zhou, Z. Sun, L.-Z. Wu, C.-H. Tunga and T. Zhang, *Nanoscale*, 2012, **4**, 6244.

11 V. Polshettiwar, R. Luque, A. Fihri, H. Zhu, M. Bouhrara and J.-M. Basset, *Chem. Rev.*, 2011, **111**, 3036.

12 (a) J. H. Jung, J. H. Lee and S. Shinkai, *Chem. Soc. Rev.*, 2011, **40**, 4464; (b) I. Ali, *Chem. Rev.*, 2012, **112**, 5073.

13 J. Gass, H. Srikanth, N. Kislov, S. S. Srinivasan and Y. Emirov, *J. Appl. Phys.*, 2008, **103**, 07B309.

14 W. Wang, S. P. Gumfekar, Q. Jiao and B. Zhao, *J. Mater. Chem. C*, 2013, **1**, 2851.

15 V. Lopez-Dominguez, J. M. Hernàndez, J. Tejada and R. F. Ziolo, *Chem. Mater.*, 2013, **25**, 6.

16 J. Gallo, N. J. Long and E. O. Aboagye, *Chem. Soc. Rev.*, 2013, **42**, 7816.

17 R. Chen, M. G. Christiansen and P. Anikeeva, *ACS Nano*, 2013, **7**, 8990.

18 Z. Karimi, L. Karimi and H. Shokrollahi, *Mater. Sci. Engin. C*, 2013, **33**, 2465.

19 H. Shao, C. Min, D. Issadore, M. Liong, T.-J. Yoon, R. Weissleder and H. Lee, *Theranostics*, 2012, **2**, 55.

20 I. Sharifi, H. Shokrollahi and S. Amiri, *J. Magn. Magn. Mater.*, 2012, **324**, 903.

21 S. Amiri and H. Shokrollahi, *Mater. Sci. Engin. C*, 2013, **33**, 1.

22 Q. Song and Z. J. Zhang, *J. Am. Chem. Soc.*, 2012, **134**, 10182.

23 A. Figuerola, R. Di Corato, L. Manna and T. Pellegrino, *Pharmacol. Res.*, 2010, **62**, 126.

24 A. J. Rondinone, A. C. S. Samia and Z. J. Zhang, *J. Phys. Chem. B*, 2000, **104**, 7919.

25 C. Liu and Z. J. Zhang, *Chem. Mater.*, 2001, **13**, 2092.

26 Q. Song and Z. J. Zhang, *J. Am. Chem. Soc.*, **2004**, 126, 6164.

27 J. Mohapatra, A. Mitra, D. Bahadur and M. Aslam, *CrystEngComm*, 2013, **15**, 524.

28 C. R. Vestal and Z. J. Zhang, *J. Am. Chem. Soc.*, 2003, **125**, 9828.

29 C. R. Vestal, Q. Song and Z. J. Zhang, *J. Phys. Chem. B*, 2004, **108**, 18222.

30 J.-T. Jang, H. Nah, J.-H. Lee, S. H. Moon, M. G. Kim and J. Cheon, *Angew. Chem. Int. Ed.*, 2009, **48**, 1234.

31 I. H. Gul, W. Ahmed and A. Maqsood, *J. Magn. Magn. Mater.*, 2008, **320**, 270.

32 S. P. Yadav, S. S. Shinde, A. A. Kadam and K. Y. Rajpure, *J. Alloys Compd.*, 2013, **555**, 330.

33 S. D. Bhame and P. A. Joya, *J. Appl. Phys.*, 2006, **99**, 073901.

34 X. Qi and D. Wu, *J. Magn. Magn. Mater.*, 2008, **320**, 666.

35 H. N. Choi, K. S. Baek, S. W. Hyun, I.-B. Shim and C. S. Kim, *IEEE Trans. Magn.*, 2009, **45**, 2554.

36 M. K. Shobana and S. Sankar, *J. Magn. Magn. Mater.*, 2009, **321**, 599.

37 R. C. Kambale, P. A. Shaikh, N. S. Harale, V. A. Bilur, Y. D. Kolekar, C. H. Bhosale and K. Y. Rajpure, *J. Alloys Compd.*, 2010, **490**, 568.

38 R. C. Kambale, P. A. Shaikh, C. H. Bhosale, K. Y. Rajpure and Y. D. Kolekar, *Smart Mater. Struct.*, 2009, **18**, 115028.

39 H. Erdemi, A. Demir and A. Baykal, *J. Inorg. Organomet. Polym.*, 2013, **23**, 690.

40 R. Topkaya, Ö. Akman, S. Kazan, B. Aktas¸ Z. Durmus and A. Baykal, *J. Nanopart. Res.*, 2012, **14**, 1156.

41 H. M. I. Abdallah, T. Moyo and J. Z. Msomi, *J. Supercond. Nov. Magn.*, 2012, **25**, 2625.

42 H. M. I. Abdallah, T. Moyo and J. Z. Msomi, *J. Supercond. Nov. Magn.*, 2011, **24**, 669.

43 J. Z. Msomi, H. M. I. Abdallah, T. Moyo and A. Lančok, *J. Magn. Magn. Mater.*, 2011, **323**, 471.

44 Y. Köseoğlu, F. Alan, M. Tan, R. Yilgin and M. Öztürk, *Ceram. Int.*, 2012, **38**, 3625.

45 H. Bayrakdar, *J. Magn. Magn. Mater.*, 2011, **323**, 1882.

46 W. Wenwei, C. Jinchao, W. Xuehang, L. Sen and H. Aigui, *Powder Technol.*, 2012, **215–216**, 200.

47 S. Laurent, D. Forge, M. Port, A. Roch, C. Robic, L. V. Elst and R. N. Muller, *Chem. Rev.*, 2008, **108**, 2064.

48 T. Javed, A. Maqsood and A. A. Malik, *J. Supercond. Nov. Magn.*, 2011, **24**, 2137.

49 A. M. Kumar, P. A. Rao, M. C. Varma, G. Choudary and K. H. Rao, *J. Modern Phys.*, 2011, **2**, 1083.

50 C. Pereira, A. M. Pereira, C. Fernandes, M. Rocha, R. Mendes, M. P. Fernández-García, A. Guedes, P. B. Tavares, J.-M. Grenèche, J. P. Araújo and C. Freire, *Chem. Mater.*, 2012, **24**, 1496.

51 M. P. Proenc□a, C. T. Sousa, A. M. Pereira, P. B. Tavares, J. Ventura, M. Vazquez and J. P. Araujo, *Phys. Chem. Chem. Phys.*, 2011, **13**, 9561.

52 P. Dutta, A. Manivannan, M. S. Seehra, N. Shah and G. P. Huffman, *Phys. Rev. B*, 2004, **70**, 174428.

53 P. Pradhan, J. Giri, G. Samanta, H. D. Sarma, K. P. Mishra, J. Bellare, R. Banerjee and D. Bahadur, *J. Biomed. Mater. Res. Part B: Appl. Biomater.*, 2007, **81B**, 12.

54 F. A. Tourinho, R. Franck and R. J. Massart, *Mater. Sci.*, 1990, **25**, 3249.

55 F. M. Al-Sogair, B. P. Operschall, A. Sigel, H. Sigel, J. Schnabl and R. K. O. Sigel, *Chem. Rev.*, 2011, **111**, 4964.

56 *Powder Diffraction: Theory and Practice*, R. E. Dinnebier and S. J. L. Billinge Eds., RSC Publishing, Cambridge, United Kingdom, 2007.

57 A. R. Denton and N. W. Ashcroft, *Phys. Rev. A*, 1991, **43**, 3161.

58 N. H. Vasoya, V. K. Lakhani, P. U. Sharma, K. B. Modi, R. Kumar and H. H. Joshi, *J. Phys. Condens.: Mater.*, 2006, **18**, 8063.

59 *Raman Spectroscopy for Nanomaterials Characterization*, C. S. S. R. Kumar Ed., Springer, Heildeberg, Germany, 2012.

60 G. V. M. Jacintho, A. G. Brolo, P. Corio, P. A. Z. Suarez and J. C. Rubim, *J. Phys. Chem. C*, 2009, **113**, 7684.

61 D. Carta, M. F. Casula, A. Falqui, D. Loche, G. Mountjoy, C. Sangregorio and A. Corrias, *J. Phys. Chem. C*, 2009, **113**, 8606.

62 M. Foerster, M. Iliev, N. Dix, X. Martí, M. Barchuk, F. Sánchez and J. Fontcuberta, *Adv. Funct. Mater.*, 2012, **22**, 4344.

63 A. Ahlawat and V. G. Sathe, *J. Raman Spectrosc.*, 2011, **42**, 1087.

64 P. Chandramohan, M. P. Srinivasan, S.Velmurugan and S. V. Narasimhan, *J. Solid State Chem.*, 2011, **184**, 89.

65 S. R. Naik and A. V. Salker, *J. Mater. Chem.*, 2012, **22**, 2740.

66 G. Shemer, E. Tirosh, T. Livneh and G. Markovich, *J. Phys. Chem. C*, 2007, **111**, 14334.

67 T. Yu, Z. X. Shen, Y. Shi and J. Ding, *J. Phys.: Condens. Matter*., 2002, **14**, L613.

68 (a) D. Varshney, K. Verma and A. Kumar, *J. Mol. Struct.*, 2011, **1006**, 447; (b) J. R. Scheffe, M. D. Allendorf, E. N. Coker, B. W. Jacobs, A. H. McDaniel and A. W. Weimer, *Chem. Mater.*, 2011, **23**, 2030.

69 R. Pązik, E. Piasecka, M. Małecka, V. G. Kessler, B. Idzikowski, Z. Śniadecki and R. J. Wiglusz, *RSC Adv.*, 2013, **3**, 12230.

70 M. A. Laguna-Bercero, M. L. Sanjuán and R. I. Merino, *J. Phys.: Condens. Matter.*, 2007, **19**, 186217.

71 (a) S. W. da Silva, F. Nakagomi, M. S. Silva, A. Franco, Jr., V. K. Garg, A. C. Oliveira and P. C. Morais, *J. Appl. Phys.*, 2010, **107**, 09B503. (b) F. Nakagomi, S. W. da Silva, V. K. Garg, A. C. Oliveira, P. C. Morais and A. Franco, Jr., *J. Solid State Chem.*, 2009, **182**, 2423.

72 P. Zinin, L. Tatsumi-Petrochilos, L. Bonal, T. Acosta, J. Hammer, S. Gilder and M. Fuller, *Am. Mineral.*, 2011, **96**, 1537.

73 C. Cannas, A. Ardu, A. Musinu, D. Peddis and G. Piccaluga, *Chem. Mater.*, 2008, **20**, 6364.

74 R. D. Waldron, *Phys. Rev.*, 1955, **99**, 1727.

75 H. Deligöz, A. Baykal, E.E. Tanrıverdi, Z. Durmus and M. S. Toprak, *Mater. Res. Bull.*, 2012, **47**, 537.

76 C. Pereira, A. M. Pereira, P. Quaresma, P. B. Tavares, E. Pereira, J. P. Araújo and C. Freire, *Dalton Trans.*, 2010, **39**, 2842.

77 C. Cacela, R. Fausto and M. L. Duarte, *Vib. Spectrosc.*, 2001, **26**, 113.

78 R. W. Berg, *Spectrochim. Acta, Part A*, 1978, **34**, 655.

79 J. M. D. Coey, *Magnetism and magnetic materials*, Cambridge University Press, Cambridge, United Kingdom, 2009.

80 A. M. Pereira, C. Pereira, A. S. Silva, D. S. Schmool, C. Freire, J.-M. Grenèche and J. P. Araújo, *J. Appl. Phys.*, 2011, **109**, 114319.

81 B. D. Plouffe, D. K. Nagesha, R. S. DiPietro, S. Sridhar, D. Heiman, S. K. Murthy and L. H. Lewis, *J. Magn. Magn. Mater.*, 2011, **323**, 2310.

82 A. Tamion, M. Hillenkamp, F. Tournus, E. Bonet and V. Dupuis, *Appl. Phys. Lett.*, 2009, **95**, 062503.

83 Y.-W. Jun, J.-H. Lee and J. Cheon, *Angew. Chem., Int. Ed.*, 2008, **47**, 5122.

84 H. Zeng, J. Li, J. P. Liu, Z. L. Wang and S. Sun, *Nature*, 2002, **420**, 395.

Captions for Figures

Figure 1. TEM micrographs of (A) $Co_{0.3}Mn_{0.7}$_M and (B) $Co_{0.7}Mn_{0.3}$_M.

Figure 2. Particle size (determined by XRD) as a function of the cobalt content for $Co_xMn_{1-x}Fe_2O_4$ synthesized with (●) MIPA and (□) NaOH. The solid lines represent the fitting obtained from equation (2).

Figure 3. (A) XRD patterns of Co_xMn_{1-x}_M nanomaterials in the 2θ range of 55–68º, highlighting the shift of the (333) and (440) Bragg reflections towards higher 2θ values upon the increase of Co(II) content. (B) Lattice parameter, *a*, as a function of the cobalt content for $Co_xMn_{1-x}Fe_2O_4$ MNPs synthesized with (●) MIPA and (□) NaOH. The lattice parameters of bulk $MnFe_2O_4$ (JCPDS card no. 10-0319) and $CoFe_2O_4$ (JCPDS card no. 22-1086) are also presented for comparison (★).

Figure 4. Raman spectra of $Co_xMn_{1-x}Fe_2O_4$ prepared with (A) MIPA and (B) NaOH in the 1000–150 cm^{-1} range.

Figure 5. Area ratio between the bands associated with the octahedral and tetrahedral sites $A_{T2g(1)}/[A_{A1g(1)}+A_{A1g(2)}]$ as a function of cobalt content.

Figure 6. (A) Room temperature *M*(*H*) curves of Co_xMn_{1-x}_M samples; solid lines: Langevin fits of *M*(*H*) curves. (B) Room temperature *M(H)* curves of Co_xMn_{1-x}_Na; inset: magnified *M*(*H*) curves.

Figure 7. Room temperature saturation magnetization (M_S) normalized by the particle size (determined by XRD) as a function of cobalt content for $Co_xMn_{1-x}Fe_2O_4$ synthesized with (●) MIPA and (□) NaOH.

Figure 8. *M*(H) curves at 5 K for samples (A) Mn_M, (B) $Co_{0.3}Mn_{0.7}$_M, (C) $Co_{0.7}Mn_{0.3}$_M and (D) Co_M.

Figure 9. (A) T_B and M_S/D_{XRD} values at 5 K as a function of the cobalt content for MIPA-based nanomaterials. (B) H_C values measured at 5 K as a function of the cobalt content for (●)MIPA and (□) NaOH sets of nanomaterials.

Figure 10. ZFC and FC curves measured under an applied magnetic field of 100 Oe of samples (A) Mn_M, (B) $Co_{0.3}Mn_{0.7}$_M, (C) $Co_{0.7}Mn_{0.3}$_M and (D) Co_M. The T_B values are highlighted by arrows (see text).

Figure 1

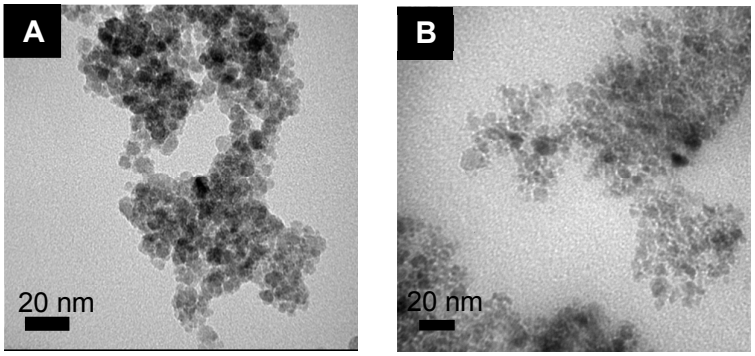

Figure 2

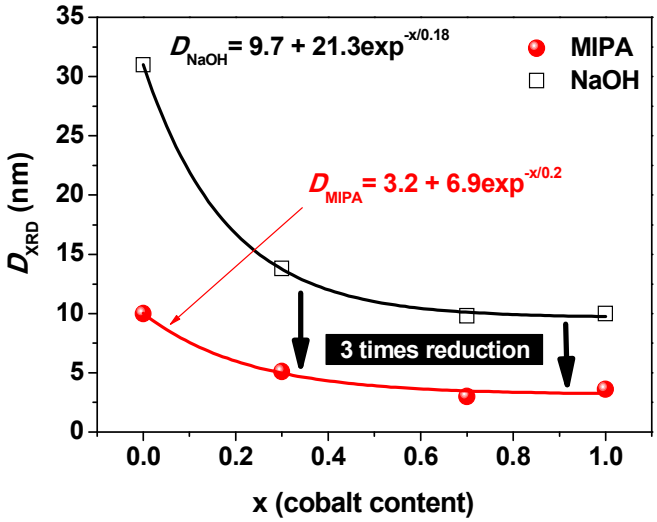

Figure 3

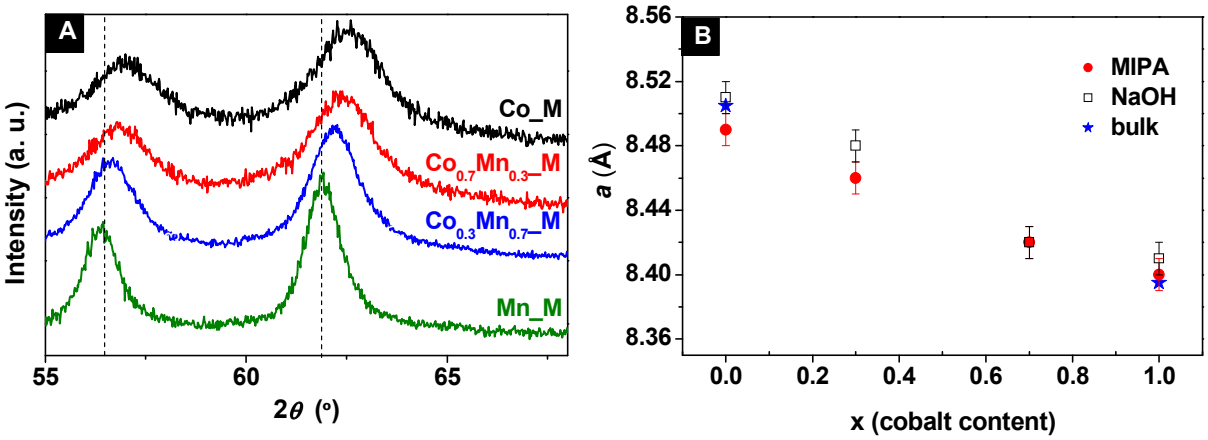

Figure 4

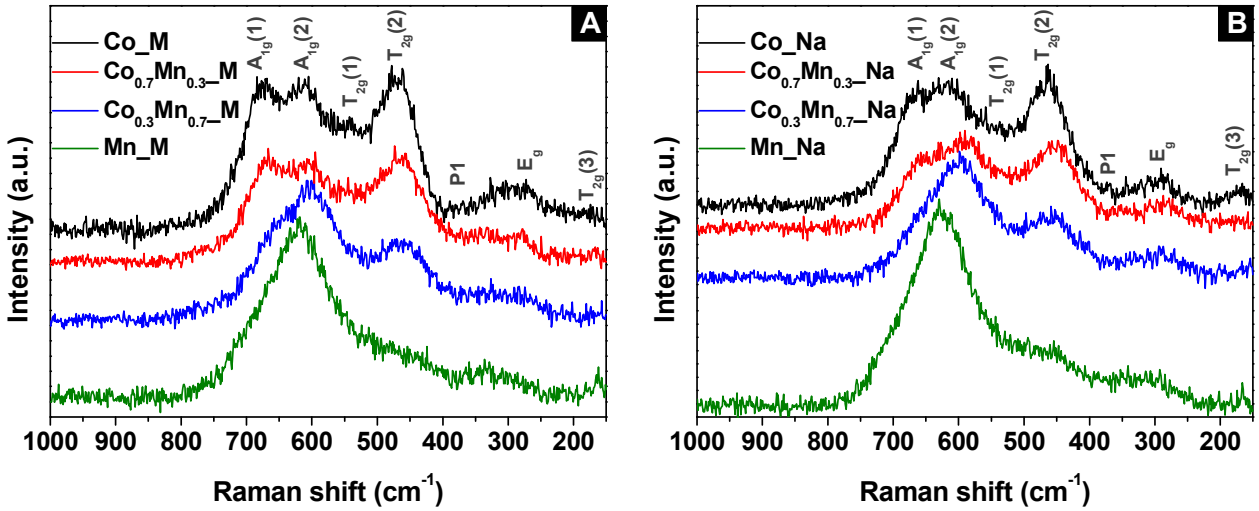

Figure 5

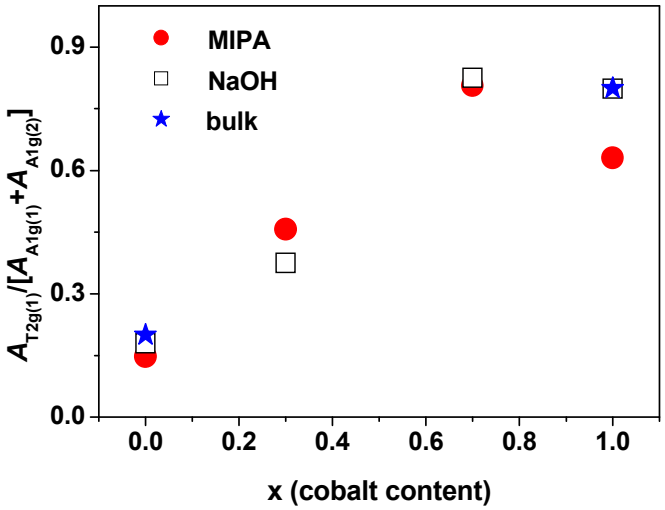

Figure 6

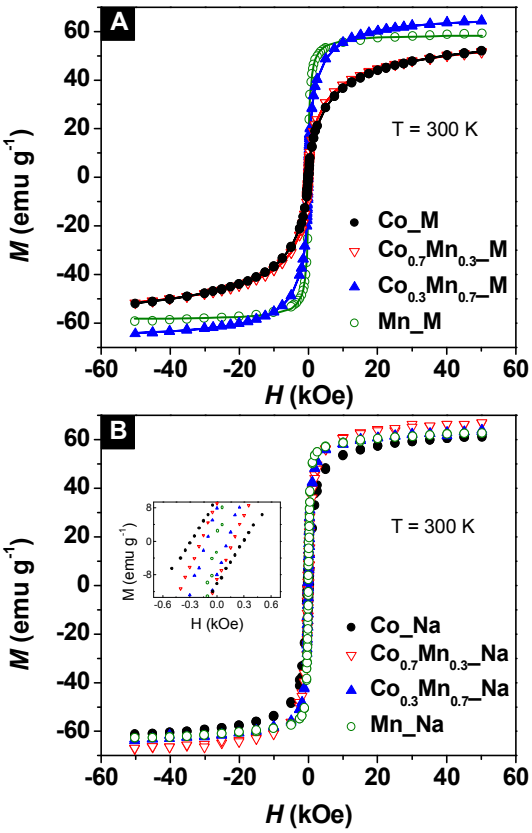

Figure 7

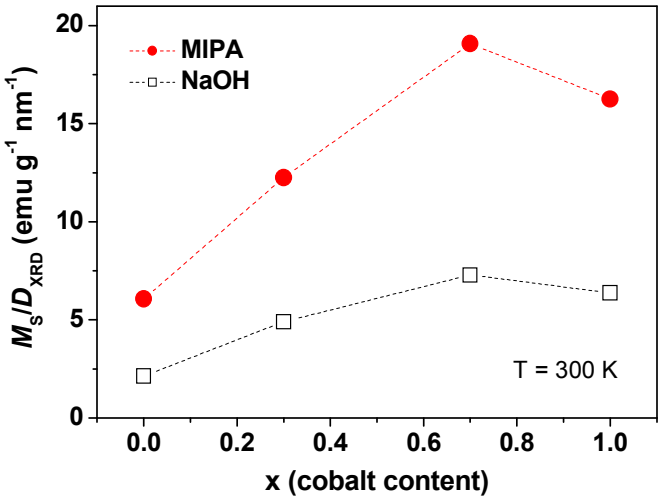

Figure 8

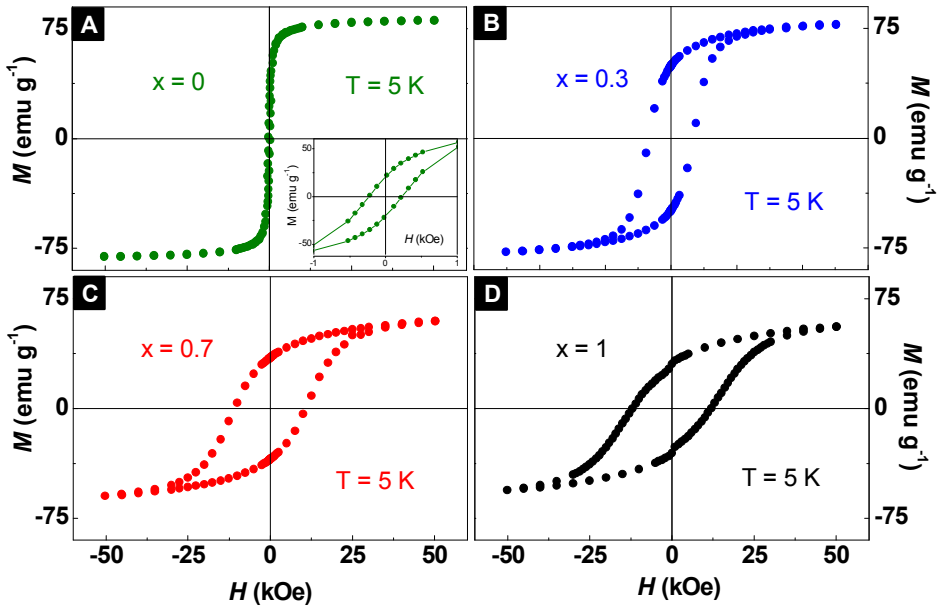

Figure 9

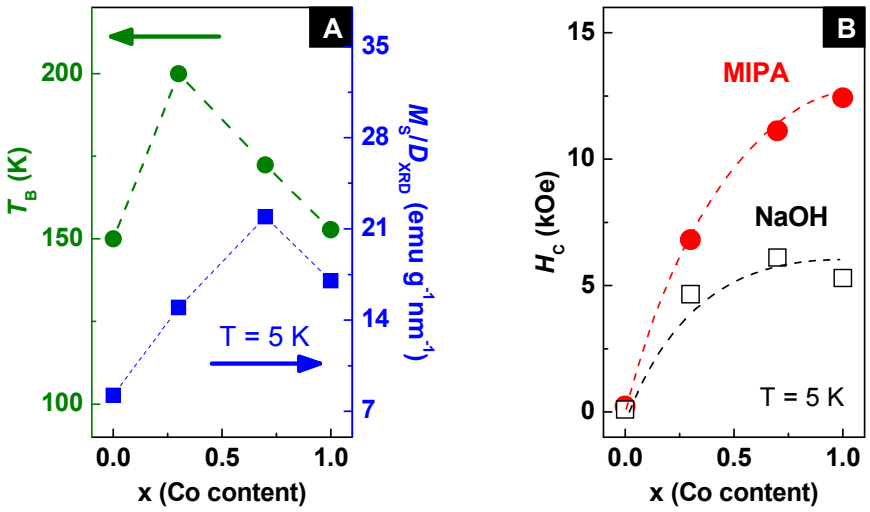

Figure 10

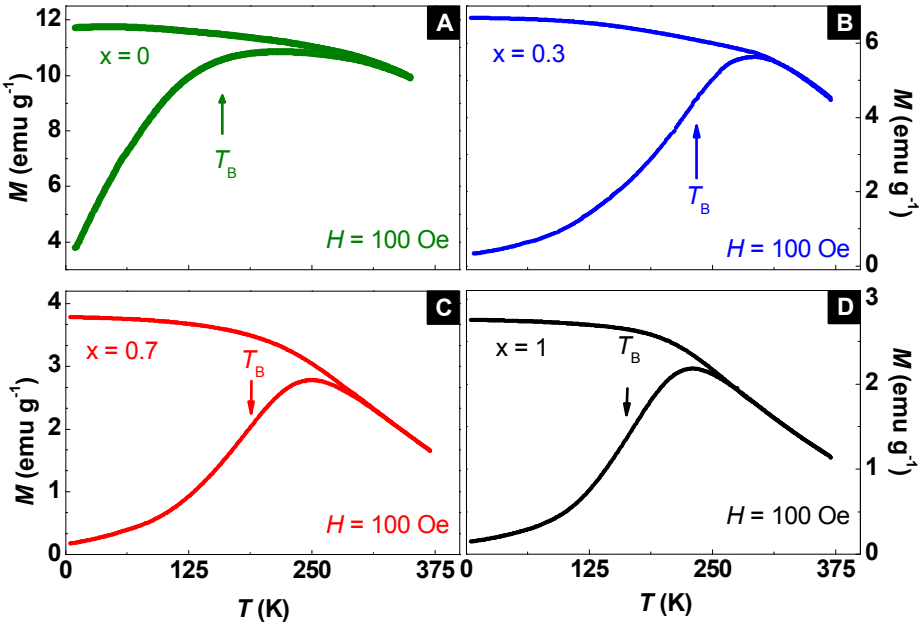

Table 1. Chemical, morphological and structural properties of $Co_xMn_{1-x}Fe_2O_4$ nanoferrites

Sample	AAS[a]		D_{TEM} (nm)[b]	σ_{TEM} (nm)[c]	D_{XRD} (nm)[d]	a (Å)[e]	D_{Lan} (nm)[f]	Total weight loss (%)[g]
	$n_{Co(II)}/n_{M(II)}$	$n_{M(II)}/n_{Fe(III)}$						
Mn_M	0.00	0.38	8.9	0.4	10.0	8.48	11.3	6.4
$Co_{0.3}Mn_{0.7}$_M	0.36	0.44	6.7	0.4	5.5	8.46	6.2	10.1
$Co_{0.7}Mn_{0.3}$_M	0.73	0.38	4.6	0.3	3.0	8.42	4.5	13.7
Co_M	1.00	0.41	4.3	0.3	3.6	8.40	4.1	14.9
Mn_Na	0.00	0.42	n.d.	n.d.	31.0	8.51	–	6.3
$Co_{0.3}Mn_{0.7}$_Na	0.37	0.43	14.4	0.4	13.8	8.48	–	7.1
$Co_{0.7}Mn_{0.3}$_Na	0.75	0.42	9.4	0.5	9.8	8.42	–	5.8
Co_Na	1.00	0.46	n.d.	n.d.	10.0	8.41	–	7.4

[a] Molar ratios determined by AAS. $n_{M(II)} = n_{Co(II)} + n_{Mn(II)}$.
[b] Average particle size estimated from TEM images, assuming log-normal size distributions; n.d., not determined.
[c] Standard deviation values obtained from the analysis of TEM images; n.d., not determined.
[d] Average crystallite size estimated by XRD, using the Williamson-Hall relation.
[e] Lattice parameter determined by XRD, using the Bragg law.
[f] Magnetic core diameter obtained by Langevin fits of the *M(H)* curves.
[g] Total weight loss quatified by TGA.

Table 2. Room temperature magnetic parameters of $Co_xMn_{1-x}Fe_2O_4$ (x = 0, 0.3, 0.7, 1) nanoferrites

Sample	M_S (emu g^{-1})[a]	M_S^{inorg} (emu g^{-1})[b]	H_C (Oe)
Mn_M	56.8	60.7	~0
$Co_{0.3}Mn_{0.7}$_M	60.6	67.5	
$Co_{0.7}Mn_{0.3}$_M	49.4	57.3	
Co_M	49.8	58.5	
Mn_Na	62.1	66.3	39
$Co_{0.3}Mn_{0.7}$_Na	62.8	67.6	120
$Co_{0.7}Mn_{0.3}$_Na	67.3	71.4	170
Co_Na	59.1	63.8	410

[a] Saturation magnetization values obtained from 1/H extrapolation.
[b] Saturation magnetization values upon TGA correction.